

# Cross-correlation frequency-resolved optical gating and dynamics of temporal solitons in silicon nanowire waveguides

Jiali Liao,<sup>1</sup> Matthew Marko,<sup>2,3</sup> Xiujuan Li,<sup>1,6</sup> Hui Jia,<sup>1</sup> Ju Liu,<sup>1</sup> Yizhou Tan,<sup>4</sup> Jiankun Yang,<sup>1</sup> Yuanda Zhang,<sup>1</sup> Wusheng Tang,<sup>1</sup> Mingbin Yu,<sup>5</sup> Guo-Qiang Lo,<sup>5</sup> Dim-Lee Kwong,<sup>5</sup> and Chee Wei Wong<sup>2,7</sup>

<sup>1</sup>College of Science, National University of Defense Technology, Changsha, Hunan 410073, China

<sup>2</sup>Optical Nanostructures Laboratory, Mechanical Engineering, Columbia University, New York 10027, USA

<sup>3</sup>Navy Air Warfare Center Aircraft Division (NAWCAD), Joint Base McGuire-Dix-Lakehurst, Lakehurst New Jersey 08733, USA

<sup>4</sup>College of Mechatronics and Automation, National University of Defense Technology, Changsha, Hunan 410073, China

<sup>5</sup>The Institute of Microelectronics, 11 Science Park Road, Singapore Science Park II, Singapore

<sup>6</sup>e-mail: xjli@nudt.edu.cn

<sup>7</sup>e-mail: cww2104@columbia.edu

Received July 8, 2013; revised September 27, 2013; accepted October 1, 2013;  
posted October 2, 2013 (Doc. ID 193505); published October 25, 2013

We demonstrate the evolution of picosecond pulses in silicon nanowire waveguides by sum frequency generation cross-correlation frequency-resolved optical gating (SFG-XFROG) and nonlinear Schrödinger equation (NLSE) modeling. Due to the unambiguous temporal direction and ultrahigh sensitivity of the SFG-XFROG, which enable observation of the pulse accelerations, the captured pulses' temporal and spectral characteristics showed remarkable agreement with NLSE predictions. The temporal intensity redistribution of the pulses through the silicon nanowire waveguide for various input pulse energies is analyzed experimentally and numerically to demonstrate the nonlinear contributions of self-phase modulation, two-photon absorption, and free carriers. It indicates that free carrier absorption dominates the pulse acceleration. The model for pulse evolution during propagation through arbitrary lengths of silicon nanowire waveguides is established by NLSE, in support of chip-scale optical interconnects and signal processing. © 2013 Optical Society of America

OCIS codes: (320.7110) Ultrafast nonlinear optics; (320.7130) Ultrafast processes in condensed matter, including semiconductors; (190.5530) Pulse propagation and temporal solitons.

<http://dx.doi.org/10.1364/OL.38.004401>

Silicon photonic nanowires (SPNWs) have been extensively studied in recent years [1–3], with the capability to tightly confine optical modes [4] and the compatibility with mature CMOS technologies [5]. A variety of photonic technologies have been demonstrated in SPNW, such as temporal soliton-effects compression [6–8], four-wave-mixing [9,10], Raman amplification [11,12], optical switching [13], all-optical modulation [14,15], all-optical wavelength conversion [16,17] and ultralow-power all-optical signal processing [18]. Group velocity dispersion (GVD) and various nonlinear effects affect the pulses' evolution, including self-phase modulation (SPM), two-photon absorption (TPA), free carrier absorption (FCA), and free carrier dispersion (FCD), not only in the time domain but also in the frequency domain [1].

Precise temporal and spectral measurements of the ultrafast pulse propagation in the SPNWs are of necessity to support its application, including recent phase-resolved short pulse measurements on-chip [19]. Cross-correlation frequency-resolved optical gating (XFROG) has been demonstrated to characterize well the complex time-frequency properties of ultrashort pulses while propagating through the semiconductor quantum optical waveguide [20] and fibers [21,22]. Here, we demonstrate cross-correlation frequency-resolved optical gating to investigate the pulse dynamics temporally and spectrally in SPNWs. With the advantage of the unambiguous temporal direction and delay, and high sensitivity compared with recent measurements by frequency-resolved optical gating (FROG), the sum frequency generation (SFG)-XFROG setup enables us to observe the pulse

acceleration experimentally. Numerical simulations based on nonlinear Schrödinger equation (NLSE) modeling with auxiliary carrier dynamics was performed to elucidate the pulse dynamics in the semiconductor media, including GVD, SPM, TPA, FCA, and FCD, and their coupled interactions on the pulse character, particularly the pulse acceleration.

The scanning electron micrograph of the silicon nanowire and the schematic experimental setup are shown in Fig. 1. The silicon nanowire waveguide is a single-mode SPNW with cross section  $A_0 = 450 \text{ nm} \times 250 \text{ nm}$ , length  $L = 4 \text{ mm}$ , and a buried oxide thickness of  $3 \mu\text{m}$ , and covered by a  $3 \mu\text{m}$  oxide layer. The oxide-cladded inverted taper couplers were adopted to improve the input–output coupling to less than 3 dB per facet.

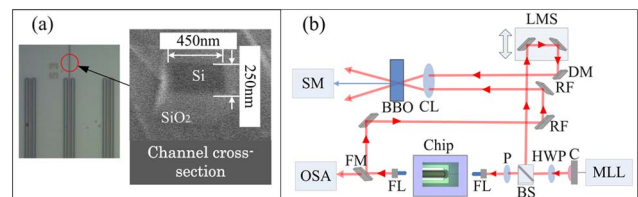


Fig. 1. Single-mode SPNW and experimental setup. (a) Scanning electron micrograph of the SPNW and (b) experimental setup with SFG-XFROG. MLL, mode-locked fiber laser; HWP, half-wave plate; C, optical collimator; BS, beam splitter; P, polarizer; FL, focus lens; FM, flip mirror; OSA, optical spectrum analyzer; RF, reflector; DM, D-shaped mirror; LMS, linear motorized stage; CL, bi-convex lens; BBO, barium borate crystal; SM, spectrometer with CCD.

The experimental setup with SFG-XFROG is shown in Fig. 1(b), in which a high-resolution sensitive grating spectrometer (Horiba JY 1000M-II with back-illumination deep-depletion CCD detector) and a 1 mm thick BBO crystal are aligned to detect pulse energies down to less than 1.0 fJ. Coherently mode-locked picosecond pulses, with a near-transform-limited 2.3 ps pulse-width and 39.1 MHz repetition rate, were generated by a PolarOnyx Saturn fiber laser tunable from 1533.5 to 1568 nm with a maximum pulse energy of 600 pJ. The coupling into and output from the SPNW was through free space to minimize the influence of fiber nonlinearities and with a linear polarizer to ensure the transverse electric polarization coupled onto the semiconductor chip. The SPNW output was also measured with an optical spectrum analyzer (OSA), to compare with the retrieved SFG-XFROG spectrum and for calibration.

Figure 2 shows the experimental and the NLSE simulation results of the output pulses for 25 pJ input pulse energy at pulse central wavelengths of 1555 and 1560 nm, in which the initial pulse intensity and phase distribution for the NLSE simulations are measured by SFG-XFROG to guarantee the uniformity of the experiments and the simulations. The parameters of NLSE for the simulations were also modified by SFG-XFROG and OSA measured data to ensure that the simulation results can predict pulse dynamics for other waveguide lengths properly. The retrieved SFG-XFROG error, in the 2D phase-retrieval solution and convergence, was determined to be less than 0.5% for each of the datasets and confirmed the setup alignment. Dispersion of the waveguide applied in the NLSE was calculated by the finite-differential time-domain algorithm [23], with the GVD  $\beta_2$  from  $-1.53$  to  $-1.49$  ps<sup>2</sup>/m for the measurement wavelength range, and the third-order dispersion  $\beta_3$  from  $-2.9 \times 10^{-3}$  to  $-4.1 \times 10^{-3}$  ps<sup>3</sup>/m.

As illustrated in Fig. 2, the pulse duration broadening ratios ( $\chi_b = T_b/T_{in}$ ,  $T_{in} = 2277$  fs, 2545 fs) are 1.82 and 1.55 for 25 pJ input pulse energy at central wavelength

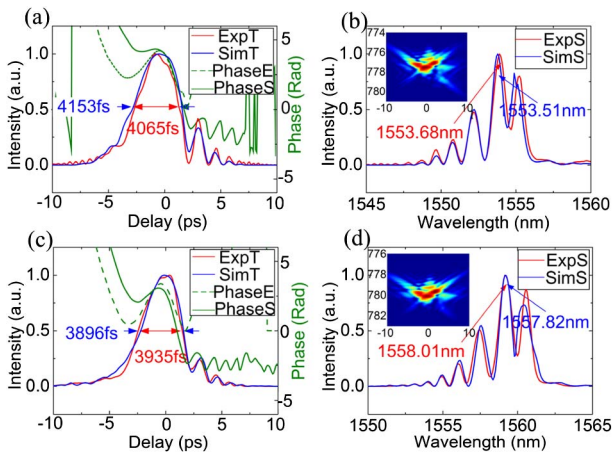


Fig. 2. Temporal intensity profile, phase distribution, and spectrum of the output pulses at 25 pJ input pulse energy. (a), (b) 1555 nm; (c), (d) 1560 nm. Red curves are experimental results, and blue curves are simulation results. The green-dotted line is the phase distribution retrieved from SFG-XFROG; the green solid line is the numerically predicted phase distribution. Insets in (b) and (d) are SFG-XFROG retrieved traces.

1550 and 1560 nm, respectively. Furthermore, the spectral centroids exhibit 0.92 and 0.87 nm Drude blueshift induced by FCD [8,24,25], relative to the 1554.60 and 1558.88 nm spectral centroids of the input pulses, which is further supported by the temporal phase distribution in the FWHM of the pulse width.

The numerical modeling shows remarkable agreement with the experimental results, including the temporal phase distribution, the temporal profile, and the spectrum, with almost the same waveform, while there are quite a few more discrepancies between the recent FROG measurements and the NLSE predictions [19]. Significantly, the SFG-XFROG measurement determines the absolute temporal centroid of the pulse, providing details of pulse dynamics analysis and phase evolution.

Figures 3(a) and 3(b), respectively, show the experimental and numerically predicted temporal and spectral intensity profiles of the 1545 nm output pulses. Due to the unambiguous temporal direction of XFROG measurements, a clear soliton acceleration along with a correlated pulse broadening with increasing input pulse energies in the time domain was clearly observed by both experiment and simulation.

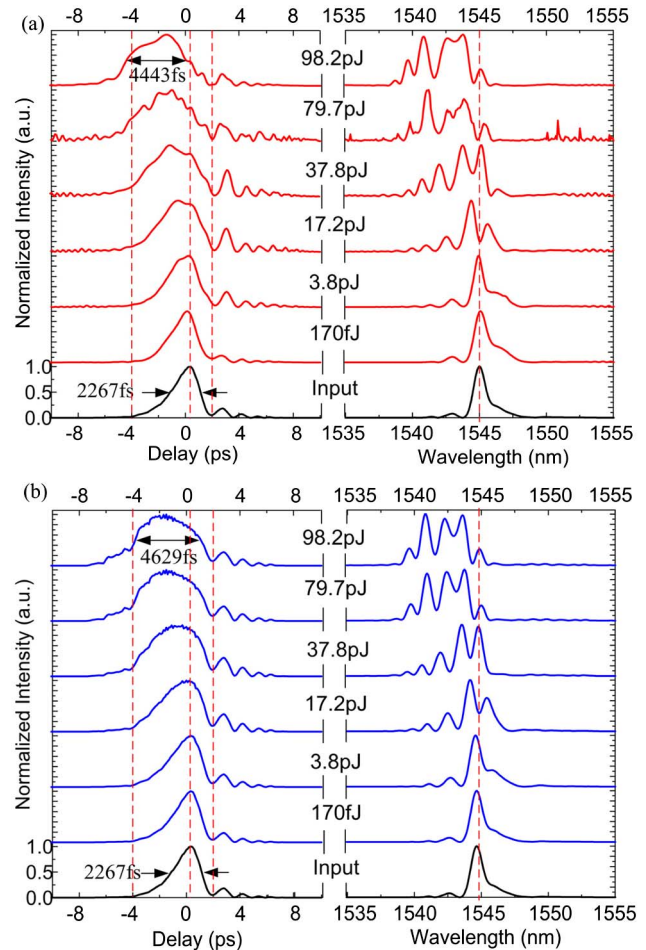


Fig. 3. Temporal and spectral intensity profiles of the output pulses for increasing coupled pulse energies from 170 fJ to 98.2 pJ. (a) Results retrieved from SFG-XFROG measurements and (b) numerically predicted results from NLSE mode simulations. Input pulse profiles are also shown in black at the figure bottom. The central labels denote the input pulse energies.

For the waveguide examined in the experiments and 2267 fs input pulses, the dispersive length  $L_D(T_0^2/|\beta_2|)$  [1], with  $T_0 = T/\Gamma$  and  $\Gamma = 1.76$  for ideal hyperbolic secant pulses, is 108 mm larger than the 4 mm sample length. The nonlinear length  $L_{NL}(1/\gamma_{\text{eff}}P_0)$  [1], where  $\gamma_{\text{eff}}$  is the effective nonlinear parameter and  $P_0$  is the pulse peak power, is from 44 mm to 76  $\mu\text{m}$  for the coupled energy range. The two characteristic lengths suggest that the impact of GVD can be neglected for the 4 mm SPNW, and the high-order temporal soliton compression phenomenon should occur. In the presence of TPA, FCA, and FCD, however, the pulse shows temporal broadening and acceleration. The measured maximum broadening ratio and acceleration are 1.96 and 1287 fs ahead, respectively, at the highest pulse energies (98.2 pJ). At the same time, the pulse spectra show blueshifts and spectral broadening from FCD and SPM, respectively [25,26]. The spectral centroid blueshifts by 2.86 nm at 98.2 pJ input pulse energy.

The measurements shown in Fig. 4(a) are for launched central wavelengths of 1545, 1550, 1555, and 1560 nm. Pulse acceleration up to about 1500 fs for different central wavelength is observed in both the SFG-XFROG measurements and NLSE simulations. For 1550 nm, Fig. 4(b) then shows the computed temporal centroids, particularly denoting the contributions of various nonlinear processes, i.e., SPM, TPA, FCA, and FCD, to extract the contribution of each nonlinear process. The results indicate that SPM and TPA hardly affect the pulse temporal centroid position, whereas FCA plays a dominant role in the pulse acceleration. FCA induces asymmetry absorption and makes the temporal pulse energy redistribute and shift to the pulse leading edge, evidence of pulse acceleration. On the other hand, effective temporal broadening is dominated by TPA [19], which attenuates the pulse temporal peak with an effectively broadened pulse base.

Figure 5 shows the temporal and spectral properties of the output pulses based on the NLSE model, parameters of which are fine-tuned and grounded by our SFG-XFROG measurements. Output pulse durations broaden to about 4 ps for 25 pJ input pulse energy with increasing length as shown in the inset zoom-in of Fig. 5(a). After 260 mm, the pulse duration shows compression, a length nearly 40 times longer than the 6.5 mm optimal distance  $Z_{\text{opt}}$ , estimated by  $L_D(0.32/N + 1.1/N^2)$  with  $N(L_D/L_{NL})$  the soliton number [7], at which point the pulse experiences a minimum width. The maximum compression

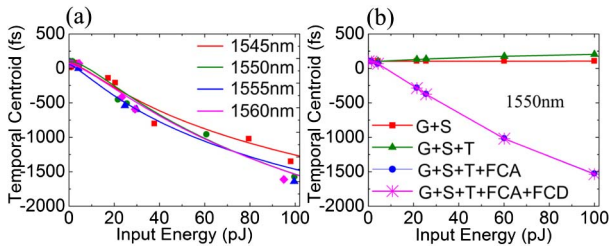


Fig. 4. Measured and simulation pulse accelerations. (a) Temporal centroid of output pulses versus input pulse energy. SFG-XFROG measurement in data points; NLSE simulations in solid lines. (b) Simulation extracted temporal centroids at 1550 nm for various cases. G, GVD; S, SPM; T, TPA.

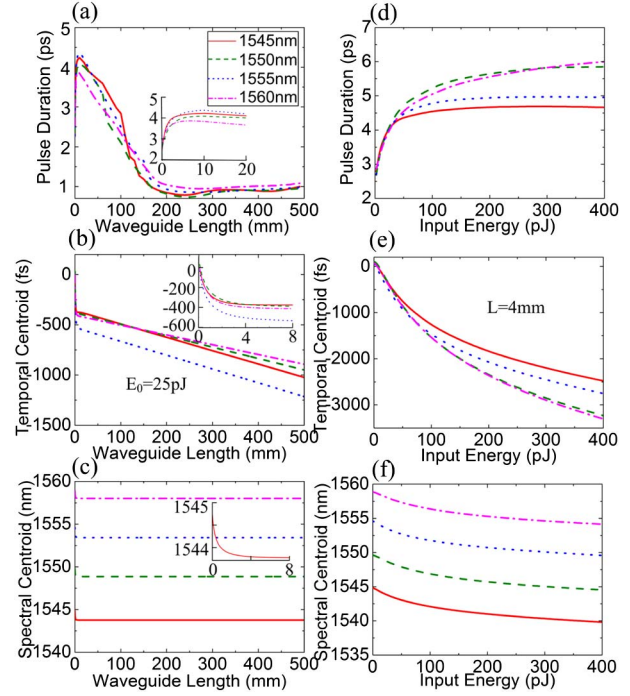


Fig. 5. Pulse properties. (a) Pulse duration, (b) temporal centroid, and (c) spectral centroid versus waveguide length up to 500 mm for 25 pJ input pulse energy. Insets: zoom-in of the initial saturation region with the same coordinate labels as the main figure. (d) Pulse duration, (e) temporal centroid, and (f) spectral centroid versus input pulse energy up to 400 pJ for 4 mm waveguide length. Wavelength assignment throughout is as shown in key in (a).

ratios ( $\chi_c = T_{\text{comp}}/T_{\text{in}}$ ) are 2.89, 3.22, 2.67, and 2.70 for the examined wavelength range. The decrease in the soliton number results from both nonlinear and linear losses, preventing compression at short length scales and high compression from large  $N$  numbers [27].

The temporal centroid of the output pulse first shifts sharply to the pulse leading edge with the increasing waveguide length to  $\sim 4$  mm, after which the pulse monotonically accelerates for increasing length, as shown in Fig. 5(b). The spectral blueshifts reach a 1 nm maximum at an  $\sim 8$  mm waveguide length, after which this is maintained through the additional increasing waveguide lengths, as shown in Fig. 5(c). The losses by the two mechanisms play an approximately equal role with a respective 4 dB for a 4 mm waveguide, then the predominance of the linear loss is enhanced with the increase in waveguide length. Therefore, the losses by linear mechanisms dominate the weakening of the intensity-squared-dependent free carrier effect in the long waveguide case.

Figure 5(d) shows the output pulse duration with increasing input pulse energy for a 4 mm waveguide. The pulse duration broadens with increasing input pulse energy, and the maximum broadening ratios are 2.07, 2.48, 2.17, and 2.36 for the central wavelength range. At the same time, the pulse temporal centroid accelerates with the increasing input pulse energy nonlinearly as shown in Fig. 5(e), and the pulse accelerations range from 2478 to 3312 fs at 400 pJ input pulse energy. Furthermore, Fig. 5(f) shows the spectral blueshift for the range of input energies. The spectral blueshifts increase

nonlinearly with the input pulse energy up to about 5 nm for the different central wavelengths examined.

The nonlinearity of the temporal pulse acceleration and spectral blueshift versus input energy result from the power attenuation by the intensity-dependent two-photon absorption and intensity-squared-dependent FCA. The losses by the nonlinear mechanisms play a significant role in the pulse dynamics at the short waveguide and high input energy cases. As a consequence, in the presence of TPA, FCA, and FCD, the pulse propagation exhibits mainly temporal broadening, acceleration, and spectral blueshift increasing nonlinearly with input pulse energy.

In summary, we have demonstrated the picosecond pulse dynamics in SPNWs by SFG-XFROG and NLSE modeling. The temporal pulse accelerations are clearly observed from the temporal direction resolved XFROG measurements and analyzed by the NLSE modeling with auxiliary carrier dynamics. This indicates that FCA dominates the temporal pulse acceleration. The numerical model, fine-tuned by our SFG-XFROG measurements, for pulse evolution was studied at varying waveguide lengths and input pulse energies, in support of understanding pulse dynamics in chip-scale optical interconnects and signal channels.

The authors acknowledge discussions with Heng Zhou and assistance from James F. McMillan and Jiangjun Zheng in performing the measurements in the Optical Nanostructures Laboratory at Columbia University. This research was funded by the National Natural Science Foundation of China (NSFC) under Grant Nos. 61070040, 61108089, 61205087, and 61107005, and by the NSF ECCS-1102257 and IGERT-1069240.

## References

1. M. A. Foster, A. C. Turner, M. Lipson, and A. L. Gaeta, *Opt. Express* **16**, 1300 (2008).
2. A. V. Velasco, P. Cheben, P. J. Bock, A. Delâge, J. H. Schmid, J. Lapointe, S. Janz, M. L. Calvo, D. Xu, M. A. F. Czyk, and M. Vachon, *Opt. Lett.* **38**, 706 (2013).
3. K. Liu, W. Xu, Z. H. Zhu, W. M. Ye, X. D. Yuan, and C. Zeng, *Opt. Lett.* **37**, 2826 (2012).
4. V. R. Almeida, C. A. Barrios, R. R. Panepucci, and M. Lipson, *Nature* **431**, 1081 (2004).
5. D. Dai and J. E. Bowers, *Opt. Express* **19**, 10940 (2011).
6. D. T. H. Tan, P. C. Sun, and Y. Fainman, *Nat. Commun.* **1**, 116 (2010).
7. M. A. Foster, A. L. Gaeta, Q. Cao, and R. Trebino, *Opt. Express* **13**, 6848 (2005).
8. C. A. Husko, S. Combrie, P. Colman, J. Zheng, A. De Rossi, and C. W. Wong, *Sci. Rep.* **3**, 1100 (2013).
9. J. B. Driscoll, N. Ophir, R. R. Grote, J. I. Dadap, N. C. Panoiu, K. Bergman, and R. M. Osgood, Jr., *Opt. Express* **20**, 9277 (2012).
10. J. F. McMillan, M. Yu, D.-L. Kwong, and C. W. Wong, *Opt. Express* **18**, 15484 (2010).
11. I. D. Rukhlenko, M. Premaratne, C. Dissanayake, and G. P. Agrawal, *Opt. Lett.* **34**, 536 (2009).
12. J. F. McMillan, M. Yu, D.-L. Kwong, and C. W. Wong, *Appl. Phys. Lett.* **93**, 251105 (2008).
13. L. Yin, J. Zhang, P. M. Fauchet, and G. P. Agrawal, *Opt. Lett.* **34**, 476 (2009).
14. K. L. Jacome, C. Poulton, J. Leuthold, and W. Freude, *Opt. Express* **15**, 5976 (2007).
15. C. A. Husko, A. De Rossi, S. Combrie, Q. V. Tran, F. Raineri, and C. W. Wong, *Appl. Phys. Lett.* **94**, 021111 (2009).
16. A. C. Turner-Foster, M. A. Foster, R. Salem, A. L. Gaeta, and M. Lipson, *Opt. Express* **18**, 1904 (2010).
17. H. Hu, H. Ji, M. Galili, M. Pu, C. Peucheret, H. C. H. Mulvad, K. Yvind, J. M. Hvam, P. Jeppesen, and L. K. Oxenløwe, *Opt. Express* **19**, 19886 (2011).
18. K. Y. Wang, K. G. Petrillo, M. A. Foster, and A. C. Foster, *Opt. Express* **20**, 24600 (2012).
19. M. D. Marko, X. Li, J. Zheng, J. Liao, M. Yu, G.-Q. Lo, D.-L. Kwong, C. A. Husko, and C. W. Wong, *Appl. Phys. Lett.* **103**, 021103 (2013).
20. N. Tsurumachi, K. Hikosaka, X.-L. Wang, M. Ogura, N. Watanabe, and T. Hattori, *J. Appl. Phys.* **94**, 2616 (2003).
21. A. Efimov and A. J. Taylor, *Appl. Opt.* **44**, 4408 (2005).
22. J. M. Dudley, X. Gu, L. Xu, M. Kimmel, E. Zeek, P. O'Shea, R. Trebino, S. Coen, and R. S. Windeler, *Opt. Express* **10**, 1215 (2002).
23. N. Kejalakshmy, A. Agrawal, Y. Aden, D. M. H. Leung, B. M. A. Rahman, and K. T. V. Grattan, *Appl. Opt.* **49**, 3173 (2010).
24. C. A. Husko, A. De Rossi, and C. W. Wong, *Opt. Lett.* **36**, 2239 (2011).
25. L. Yin and G. Agrawal, *Opt. Lett.* **32**, 2031 (2007).
26. O. Boyraz, T. Indukuri, and B. Jalali, *Opt. Express* **12**, 829 (2004).
27. P. Colman, C. Husko, S. Combrié, I. Sagnes, C. W. Wong, and A. De Rossi, *Nat. Photonics* **4**, 862 (2010).